Revision 2

Word count ~6580

Subsolidus breakdown of armalcolite: Constraints on thermal effects during shock lithification of lunar regolith

TIAN-RAN TRINA DU[1], AI-CHENG ZHANG[1,2]*, JIA-NI CHEN[1], AND YUAN-YUN WEN[3]

[1]State Key Laboratory for Mineral Deposits Research, School of Earth Sciences and Engineering, Nanjing University, Nanjing 210023, China

[2]CAS Center for Excellence in Comparative Planetology, Hefei 230026, China

[3]Center for Lunar and Planetary Sciences, Institute of Geochemistry, Chinese Academy of Sciences, Guiyang 266071, China

*Corresponding author. E-mail: aczhang@nju.edu.cn

For submisstion to **American Mineralogist**

ABSTRACT

Shock lithification of regolith breccias is a ubiquitous process on the surfaces of airless planetary bodies and may induce thermal effects, including melting on regolith breccia minerals. However, potential thermal effects on lithic and mineral clasts in regolith breccias were seldom quantitatively constrained. Here, we report two types of micro-textures of armalcolite [$(Mg,Fe^{2+})Ti_2O_5$] in an Mg-suite lithic clast from lunar regolith breccia meteorite Northwest Africa 8182. One type of armalcolite contains oriented fine-grained ilmenite grains; the other occurs as an aggregate of ilmenite, rutile, spinel, and loveringite. We propose that the two types of micro-textures formed through subsolidus breakdown of armalcolite by different processes. The formation of ilmenite inclusions in armalcolite is related to slow cooling after the solidification of its source rock; however, the ilmenite-rutile-spinel-loveringite aggregates probably formed during the shock lithification event of NWA 8182. The results indicate that the temperature at the margin of lithic clasts could be raised up to at least 600 ^{o}C during strong shock lithification of lunar regolith and has profound thermal effects on the mineralogical and isotopic behaviors of lithic and mineral fragments in lunar regolith breccias.

Keywords: Armalcolite, subsolidus breakdown, shock lithification, lunar regolith, lunar meteorite

INTRODUCTION

Lunar regolith is loose, fine-grained material on the surface of the Moon. It holds key information about the formation and evolution of the Moon and the interaction between surface materials and harsh space environments (Heiken et al. 1991). Lunar regolith is inevitably subjected to cycles of fragmentation, comminution, agglutination, compaction, and lithification during its long-term residence on the surface of the Moon. Shock lithification is the major process that generates regolith breccias from fine-grained regolith material (Kieffer 1975; Spray 2016). Kieffer (1975) has qualitatively divided shock lithification into strong and weak shock lithification, based on the presence or not of shock-induced glass and new crystalline phases, respectively. The shock metamorphic conditions of strongly shock-lithified breccias may vary from 5–10 GPa to near or in excess of 60 GPa (Kieffer 1975; Schaal and Hörz 1980). Many lunar meteorites and Apollo lunar breccias formed by strong shock lithification (Kieffer 1975; Taylor et al. 1991; Spray 2016; Zhang et al. 2021). The high-temperature melt generated during strong shock lithification can have profound thermal effects on the mineralogical features of the lithic and mineral fragments in lunar regolith breccias (e.g., Gibbons et al. 1975; Simonds et al. 1976; Zhang et al. 2021; and references therein).

Previous investigations have largely discussed the potential thermal effects during strong lithification of lunar regolith, such as fusion-crystallization (Warner 1972; Warner et al. 1973), sintering (Simonds 1973; Uhlmann et al. 1975), diffusion and overgrowth formation (Warner 1972), thermally activated degassing (Williams 1972), and formation of high-temperature and high-pressure minerals (Zhang et al. 2021). However, most of these investigations focused on the thermal effects on the fine-grained, matrix phases among coarse-grained lithic and mineral fragments. In contrast, potential shock-lithification thermal effects on lithic and mineral fragments in lunar breccias, which are usually the major materials to be studied to constrain the geological processes and evolution history of lunar rocks, are less constrained.

Armalcolite is a Ti-Mg-Fe oxide mineral (theoretical formula $Mg_{0.5}Fe_{0.5}Ti_2O_5$) discovered in Apollo 11 samples, with the pseudobrookite structure (Anderson et al. 1970). It is present in many Apollo basaltic samples and lunar meteorites (e.g., Anderson et al. 1970; Haggerty et al. 1970; Steele and Smith 1972; Haggerty 1973; El Goresy et al. 1974; Williams and Taylor 1974; Stanin and Taylor 1979; Treiman and Gross 2015; Zhang et al. 2020). Previous experimental investigations based on the TiO_2-FeO system have demonstrated that high-temperature nonstoichiometric ferropseudobrookite [$Fe_{(1+2x/3)}Ti_{(2-x/3)}O_5$ or $Fe_{(1-x)}Ti_{(2+x/2)}O_5$, x=0–1], which is isostructural with armalcolite, will experience two-stage subsolidus breakdown reactions with decreasing temperature (Lindsley 1991). At high temperatures, nonstoichiometric ferropseudobrookite may transform into stoichiometric ferropseudobrookite ($FeTi_2O_5$) and ilmenite/rutile, depending on its initial compositions. At lower temperatures, ferropseudobrookite becomes unstable and will break down into ilmenite and rutile (Lindsley 1991). Experiments studying the breakdown reaction of armalcolite into ilmenite and rutile have also been conducted to constrain the effects of major- and minor-elements, pressure, and oxygen fugacity on the stability of armalcolite (Lindsley et al. 1974; Kesson and Lindsley 1975; Friel et al. 1977). Various stability at different temperatures implies that armalcolite could play an important role to constrain the thermal evolution of its host rocks.

Northwest Africa (NWA) 8182 is a brecciated lunar meteorite (Ruzicka et al. 2017). Zhang et al. (2021) proposed that it experienced strong shock lithification on the

DOI: https://doi.org/10.2138/am-2022-8790. http://www.minsocam.org/

lunar surface, based on the high abundance of shock-induced glass and the presence of Mg,Fe-rich tissintite [theoretical formula $(Ca,Na,\square)AlSi_2O_6$], a high-pressure mineral (Ma et al. 2015). Armalcolite has been observed in an Mg-suite lithic clast (Clast-20) from this meteorite (Zhang et al., 2020). In the present study, we report the micro-textures of the two subsolidus breakdown reactions of armalcolite in Clast-20. One of the breakdown micro-textures can be attributed to the thermal effects on lithic clasts during shock lithification of lunar regolith.

ANALYTICAL METHODS

Petrographic observations in the present study were mainly carried out with the Zeiss Supra 55 field emission scanning electron microscope (FE-SEM) at Nanjing University, Nanjing, China. The SEM instrument was operated at an accelerating voltage of 15 kV in the backscattered electron (BSE) imaging mode. A silicon-drift detector energy dispersive spectrometer (SDD-EDS) attached on the FE-SEM instrument was used to obtain semi-quantitative compositions of minerals and X-ray elemental maps. For the X-ray elemental mapping of the lithic clast, the accelerating voltage was 15 kV as well. Each pixel is about 1.4 μm and the dwell time for each pixel is 10 μs.

Chemical compositions of minerals in the polished section were measured with the JEOL 8530 field emission electron probe microanalyzer (FE-EPMA) at Nanjing University. The EPMA instrument was operated at a 15-kV accelerating voltage and a 20-nA beam current. A focused mode was used for the measurements on grains larger than 2 μm in diameter; a defocused beam of 3 μm in diameter was used for the measurements on plagioclase and multiple phase aggregates. Peak and background measurement times for all elements in this study are 20 s and 10 s, respectively. Natural and synthetic materials were used as standards for concentration calibration. All EPMA data were reduced with the atomic number-absorption-fluorescence (ZAF) procedure. The detection limit for TiO_2 is approximately 0.03 wt% and the detection limits for oxides of other elements are better than 0.02 wt%.

Two ultrathin foils were prepared with the FEI Scios focused ion beam scanning electron microscope (FIB-SEM) instrument at the Institute of Geochemistry, Chinese Academy of Sciences, Guiyang, China. Final thickness of the foils is approximately 100 nm. Mineral identifications and texture observations of the foils were performed with the FEI Tecnai F20 transmission electron microscope (TEM) at Nanjing University. The F20 TEM instrument was operated at a 200-kV accelerating voltage. Chemical compositions and elemental mappings were measured under STEM mode by an energy dispersive X-ray detector installed on the F20 TEM instrument. Both TEM mode and high angle annular dark-field scanning transmission electron microscope (HAADF-STEM) mode were used to observe micro-textures and petrography. The minerals in the FIB sections were identified by combining the selected area electron diffraction (SAED) patterns of minerals or Fast Fourier Transfer (FFT) patterns of high-resolution TEM images and STEM-EDS data.

RESULTS

NWA 8182 shows a typical breccia texture with abundant lithic clasts and mineral fragments cemented by glassy matrix. Shock-induced glass is common in the fine-grained regions among lithic clasts and mineral fragments and contains abundant vesicles (Fig. 1). Magnesium,Fe-rich tissintite, is also commonly observed in a few thin glassy regions and at the margin of wide glassy regions (Zhang et al. 2021). The petrography and mineralogy of the armalcolite-bearing lithic clast (Clast-20) in NWA 8182 has been reported by Zhang et al. (2020). Therefore, here, we briefly describe the petrography and mineralogy of this clast and mainly focus on the micro-textures of armalcolite.

Clast-20 is a 1.3 mm × 0.7 mm Mg-suite lithic clast surrounded by vesicle-rich glassy matrix. Approximately two thirds of the glassy matrix surrounding this clast is relatively wide (50–100 μm) and contains fine-grained tissintite aggregates along the interface with Clast-20. Mineral fragments and vesicles are common in this glassy region. The rest of the glassy matrix surrounding Clast-20 is relatively thin (less than 30 μm in width) and contains no tissintite, although rounded vesicles are also observed. Clast-20 consists mainly of plagioclase (55.8 vol%; 50–250 μm in size), olivine (28.2 vol%; 10–230 μm in size), pyroxene (14.4 vol%; 10–90 μm in size) and shows a subophitic texture (Fig. 2a). No chemical variations were observed for olivine ($Fo_{86.0–86.6}$, n=5) and pyroxene ($En_{84.2–84.9}Fs_{12.3–12.7}Wo_{2.5–3.1}$, n=8; $En_{48.8–51.0}Fs_{5.1–6.3}Wo_{42.6–46.2}$, n=7). Plagioclase ($An_{87.5–91.1}Ab_{8.5–11.6}Or_{0.4–0.9}$, n=2) has partly transformed into glass, with the untransformed regions characterized by the presence of irregular fractures. Enstatite and augite in Clast-20 occur either as discrete grains or form an intergrowth texture. Zhang et al. (2020) suggested a two-pyroxene equilibrium temperature of approximately 1030 ^{o}C (Wells 1977; Brey and Kohler 1990). Discrete oxide minerals in Clast-20 are armalcolite, chromite, loveringite [$(Ca_{0.99}Na_{0.01})_{\Sigma1.00}(Ti_{14.22}Fe_{2.06}Cr_{2.01}Mg_{1.20}Zr_{0.54}Al_{0.49}Ca_{0.21}Y_{0.05}Mn_{0.04}Ce_{0.03}Si_{0.03}La_{0.01}Nd_{0.01}Dy_{0.01})_{\Sigma20.91}O_{38}$, Zhang et al. 2020], ilmenite, and rutile. Armalcolite and chromite are common in Clast-20 (Fig. 2b); but only a few discrete ilmenite and rutile grains were observed. The ilmenite grains have an Mg# value [Mg#=Mg/(Mg+Fe) in mole fraction] of 0.30–0.37 (Zhang et al. 2020). A few Ca-phosphate and monazite grains are also present in Clast-20.

Armalcolite appears to be evenly distributed in Clast-20 (Fig. 2b), mostly occurring as discrete grains (5–25 μm in size), but a few form intergrowths with loveringite (Zhang et al. 2020). Most armalcolite grains contain submicrometer ilmenite inclusions (<0.5 μm in size; Fig. 3). Within a few armalcolite grains, the tiny ilmenite grains show an oriented distribution (Figs. 3a and 3b). The armalcolite grains show either homogeneous or slightly heterogeneous Z-contrasts in BSE images (Fig. 3). Chemically, the armalcolite grains with and without ilmenite inclusions show essentially identical compositions, with the Mg# value varying from 0.54 to 0.61 (Table 1), which is consistent with those reported in Zhang et al. (2020). The Al_2O_3 and Cr_2O_3 contents in armalcolite are 0.3–1.1 wt% and 1.0–2.0 wt%, respectively. One FIB section (labelled as FIB-1) was cut from an armalcolite grain with varying Z-contrasts in BSE image (Fig. 3c), which is approximately 10 μm away from the tissintite- and vesicle-bearing glassy matrix. TEM observations of FIB-1 show that the whole grain is an aggregate of 100–800 nm euhedral armalcolite (93.1 vol%) that shows a triple-junction texture in some regions and ilmenite (6.9 vol%) (Fig. 4). No other phases, such as rutile and spinel, were observed. The armalcolite grains in the FIB section have roughly similar orientations with a misorientation of <5°. Ilmenite (50–100 nm) occurs as an interstitial phase between the armalcolite grains (Fig. 4a). The STEM-EDS analyses reveal that the ilmenite grains are relatively Fe-rich (Mg#=0.37–0.38; Table 2), generally similar to those of individual ilmenite grains in Clast-20 (Mg#=0.39, Zhang et al. 2020).

In the present study, we observe two special armalcolite grains (termed pseudo-armalcolite) of approximately 5 × 15 μm at the margin of Clast-20 (Fig. 5). Both grains are less than 10 μm away from the tissintite- and vesicle-bearing glassy matrix, which is approximately 100 μm in width (Figs. 5a and 5b). One grain is in direct contact with glassy matrix while the other is included in an anorthite grain which contains a large elongate vesicle (Figs. 5a and 5b). These two pseudo-armalcolite grains show complex micro-textures in BSE images (Figs. 5c and 5d), different from those of normal armalcolite grains shown in Fig. 3. However, defocused-beam EPMA analyses reveal that they have major and minor element contents generally similar to those of normal armalcolite grains in Clast-20 (Table 1). Low-resolution SEM-EDS elemental mappings show that the pseudo-armalcolite grains contain an Al,Cr-rich phase (Fig. 6). One FIB section (labelled as FIB-2) was cut from one of the pseudo-armalcolite grains, which is enclosed in anorthite (Fig. 7b). Our TEM observations reveal that the pseudo-armalcolite grain is composed mainly of rutile (43.4 vol%), ilmenite (41.6 vol%), and spinel (11.3 vol%) with minor loveringite (2.7 vol%) (Figs. 7 and 8). The ilmenite and rutile grains have similar grain sizes (200–800 nm) and show a triple-junction texture (Figs. 7a and 7d), while the spinel grains are between 80–300 nm. The loveringite grains has similar grain sizes and shapes to ilmenite, rutile, and spinel (Fig. 7). The STEM-EDS analyses show that the Mg# values of ilmenite in the pseudo-armalcolite grains are 0.53–0.54 (Table 2). The spinel grains in the FIB-2 section are highly magnesian (Mg#=0.80) and contain some amounts of TiO_2 and Cr_2O_3 (Fig. 9). The anorthite grain enclosing pseudo-armalcolite is mainly crystalline, but contains many parallel amorphous lamellae of 5–10 nm in width (Fig. 10).

DISCUSSION

In Apollo lunar samples, armalcolite is closely associated with other Ti-rich oxide minerals, such as ilmenite, rutile, and ulvöspinel (e.g., Anderson et al. 1970; Haggerty, 1973; El Goresy et al. 1974; Williams and Taylor 1974). In most cases, armalcolite and ilmenite either occur as discrete grains or form a core-mantle texture. Both of them could crystallize as primary phases from magmas or form through reactions between early-crystallized phases and silicate melts (Haggerty 1973; El Goresy et al. 1974; Williams and Taylor 1974; Thacker et al. 2009). The various textural relationships between armalcolite and ilmenite in Apollo lunar samples have been attributed to differences in bulk rock compositions, cooling rates, and oxygen fugacity (Haggerty 1973; El Goresy et al. 1974; Papike et al. 1974; Stanin and Taylor 1979; Thacker et al. 2009). In contrast, although it is well known from phase diagrams of the Fe-TiO_2 and MgO-Fe-Ti-O systems that armalcolite may experience two-stage subsolidus breakdown reactions with decreasing temperature (Lindsley et al. 1974; Lindsley 1991), conclusive evidence for subsolidus breakdown of armalcolite has seldom been reported in Apollo lunar samples (e.g., Haggerty 1973). Haggerty (1973) reported that a 350 μm × 250 μm pseudomorph armalcolite grain in Apollo 14 polymict breccia 14321 has decomposed into the assemblage rutile + ilmenite in approximately a 1:1 ratio with minor chromite. He suggested that the polymict breccia must have suffered high-temperature reheating (>1000 ^{o}C), but did not discuss what process caused the high-temperature reheating event (Haggerty 1973).

In the present study, we observe that two types of crystal-scale micro-textures of armalcolite grains occur in an Mg-suite lithic clast (Clast-20): oriented ilmenite inclusions in normal armalcolite grains and ilmenite-rutile-spinel intergrowths in pseudo-armalcolite grains. The mineral assemblages in the two types of armalcolite micro-textures are identical to the expected assemblages of two-stage breakdown reactions of armalcolite, respectively (Lindsley et al. 1974; Lindsley 1991). Based on the micro-textures and similar mineral assemblages, we propose that the two types of micro-textures can be attributed to different breakdown reactions of pre-existing Ti-deficient armalcolites (Fig. 11). The ilmenite inclusions in armalcolite are the breakdown (exsolution) products of a pre-existing phase (probably Ti-deficient armalcolite). One may argue that when temperature cools to the eutectic, armalcolite and ilmenite will form simultaneously. However, differing from a simple armalcolite-ilmenite system, in a Ti-rich silicate melt, it dose not necessitate that eutectic armalcolite and ilmenite form an intimate intergrowth texture or inclusion texture. It is more likely that co-crystallizing armalcolite and ilmenite form discrete grains or simply associated assemblage of subhedral to euhedral grains. However, this contrasts with the observations in the present study that discrete ilmenite grains are rare and ilmenite occurs mainly as fine-grained inclusions in armalcolite. Therefore, the micro-texture that oriented ilmenite grains are included in armalcolite is more consistent with a subsolidus breakdown reaction of Ti-deficient armalcolite, rather than eutectic crystallization of armalcolite and ilmenite.

The coexisting ilmenite and rutile in the pseudo-armalcolite grains could be the complete breakdown products of pre-existing armalcolite. The roughly 1:1 ratio for ilmenite and rutile in the pseudo-armalcolite grains supports this explanation (Haggerty

DOI: https://doi.org/10.2138/am-2022-8790. http://www.minsocam.org/

1973). Spinel in the pseudo-armalcolite grains could be a byproduct of the breakdown reaction (Haggerty 1973; Kesson and Lindsley 1974), considering that armalcolite in Clast-20 contains small amounts of Al_2O_3 and Cr_2O_3 but the two major breakdown products ilmenite and rutile contain no Al and Cr. A few loveringite grains are observed in the pseudo-armalcolite shown in FIB-2 section. Loveringite is an important accessory mineral in Clast-20 (Zhang et al. 2020). It also forms intergrowths with armalcolite (Fig. 3d), suggesting that the loveringite grains in FIB-2 section might be of relict origin. However, we notice that the armalcolite grains in Clast-20 and some armalcolite grains from Apollo lunar samples contain 0.3–0.5 wt% CaO (Zhang et al. 2020; Haggerty 1973; El Goresy et al. 1974). When these Ca-bearing armalcolite grains break down into ilmenite, rutile, and chromite, Ca does not incorporate into these oxide minerals. Instead, the presence of loveringite, which is Ca-rich, can account for the fate of Ca in armalcolite during the breakdown reaction. If this is the case, the loveringite grains in FIB-2 section would have a breakdown origin. The loveringite grains in FIB-2 section have similar sizes to ilmenite and rutile, which seems to be consistent with the breakdown origin. One significance of a breakdown origin of loveringite would be that loveringite is more stable than armalcolite at relatively low temperatures.

Previous experimental investigations have revealed that the stability of armalcolite is a function of Mg# value, abundances of minor elements (such as Al^{3+}, Cr^{3+}, and Ti^{3+}), oxygen fugacity, and pressure (Lindsley et al. 1974; Kesson and Lindsley, 1975; Friel et al. 1977). Higher concentrations of MgO, Al_2O_3, Cr_2O_3, and Ti_2O_3 can stabilize armalcolite to lower temperatures (Lindsley et al. 1974; Kesson and Lindsley 1975). At low pressures (e.g., near or less than 1 kbar), the breakdown temperature for pure $Fe_{0.5}Mg_{0.5}Ti_2O_5$ to ilmenite and rutile is approximately 1010 ^oC (Lindsley et al. 1974). However, the breakdown to ilmenite and rutile of armalcolite with an Mg# value of 0.6 begins above 950 ^oC and would be complete roughly at 780–800 ^oC (Lindsley et al. 1974). The presence of minor trivalent cations (Al^{3+}, Cr^{3+}, and Ti^{3+}) can also extend the stability of armalcolite to a lower temperature by 50–100 ^oC (Kesson and Lindsley 1975). It means that Al^{3+},Cr^{3+},Ti^{3+}-bearing armalcolite (Mg#=0.6) will begin to break down at a temperature around 850–900 ^oC. Interestingly, Kesson and Lindsley (1975) noted that the experiements at 800 ^oC and 770 ^oC showed no breakdown reaction of armalcolite (Mg#=0.5) even after run durations of four months. This probably implies that the breakdown reaction of armalcolite is hampered by kinetics at temperatures of <800 ^oC, although that armalcolite is thermodynamically unstable below 950 ^oC. Therefore, we suspect that the breakdown of armalcolite to ilmenite and rutile should be complete above 800 ^oC. Increasing pressure also has a tendency of raising the breakdown temperature of armalcolite (Lindsley et al. 1974; Friel et al. 1977). Based on the experiements on karooite ($MgTi_2O_5$), Lindsley et al. (1974) suggested that the armalcolite stability field probably disappears entirely at some pressure greater than 2 GPa. However, all the experiements studying the effect of pressure on the stability of armalcolite have been performed at temperatures of $\geq$900 ^oC (Lindsley et al. 1974; Friel et al. 1977). It remains unknown whether increasing pressure would be helpful to overcome the kinetic effect at temperatures of $<$900 ^oC for breakdown of armalcolite.

The different mineral assemblages imply that the micro-textures of normal armalcolite grains and pseudo-armalcolite grains in Clast-20 should have formed in one uneven reheating event or two different events. The exsolution texture of pyroxene grains in Clast-20 indicates that the source rock of Clast-20 probably experienced slow cooling at ~1030 ^{o}C (Zhang et al. 2020). Different from typical plutonic Mg-suite rocks that are usually composed of coarse-grained minerals (Shearer et al. 2015), the constituent minerals in Clast-20 are generally fine-grained. This difference indicates that Clast-20 is not a fragment from typical plutonic Mg-suite rocks. Clast-20 probably crystallized either from a thin, Mg-suite dyke or from an impact melt of an originally plutonic Mg-suite rock. However, it is difficult to distinguish the possible origins for the source rock of Clast-20 based on the observations in the present study. The other thermal event that Clast-20 experienced is shock lithification, indicated by the presence of tissintite- and vesicle-bearing glass surrounding Clast-20 (Zhang et al. 2021; this study). In the following sections, we will discuss the potential correlations between the armalcolite micro-textures and the two thermal events. The slow cooling of the source rock of Clast-20 at ~1030 ^{o}C can account for not only the exsolution of tiny ilmenite from normal armalcolite at a temperature higher than 850–900 ^{o}C, but also the consistency of Mg# values of discrete ilmenite grains and those within armalcolite. However, slow cooling of a magma/melt usually has a linear temperature distribution at a scale much larger than Clast-20 of millimeter scale; it cannot account for coexistence of two types of micro-textures of armalcolite in Clast-20 and different Mg# values between the tiny ilmenite inclusions within normal armalcolite and those within pseudo-armalcolite (Table 2).

An impact event can produce heterogeneous temperature rises at micrometer scale (Sharp and DeCarli 2006). If both types of micro-textures of armalcolite observed in Clast-20 were the products of the shock lithification event, the widespread presence of armalcolite with ilmenite inclusions would require a rather high post-shock temperature (>850–900 ^{o}C) across the clast. According to Table 6 of Stöffler et al. (2018), an impact event with such a high post-shock temperature, however, would produce maskelynite and lead to mixed melt of plagioclase and pyroxene, which are not observed in Clast-20. In addition, a breakdown to ilmenite and rutile would be expected for most of the armalcolite grains, since at high pressures and temperatures around >850–900 ^{o}C armalcolite is not stable (Lindsley et al. 1974; Friel et al. 1977). Therefore, it is unlikely that both types of micro-textures of armalcolite in Clast-20 were produced by a common impact event.

Instead, the formation of ilmenite-rutile-spinel assemblage in pseudo-armalcolite could be attributed to the shock-lithification event of NWA 8182, while the exsolution of ilmenite in the majority of armalcolite in Clast-20 could be due to slow cooling of its source rock as discussed above. During shock lithification or even shortly after pressure relase, the margin of Clast-20 could have been heated up to a certain higher temperature than the interior. Under shock-induced high temperatures, the two pseudo-armalcolite grains broke down to ilmenite, rutile, spinel, and even loveringite. Meanwhile, such breakdown reaction did not take place for other armalcolite grains in Clast-20, probably due to low temperatures under which the kinetics cannot be overcome, even if the shock pressure might be high.

Based on the presence of abundant vesicular glass, NWA 8182 probably experienced shock metamorphism of near or in excess of 40 GPa (Schaal and Hörz 1980). The presence of tissintite along the margin of Clast-20 indicates a high pressure at least of 4.5–5 GPa (Rucks et al. 2018, 2019). It is likely that the breakdown of armalcolite to ilmenite and rutile took place when the pressure was still loaded. However, due to the lack of knowledge about the high-pressure (>4.5 GPa) and high-temperature behavior of armalcolite, it is difficult to directly constrain the temperature range for the breakdown of the pseudo-armalcolite grains. TiO_2 has various polymorphs, such as rutile, anatase, brookite, TiO_2-II (Wu et al. 2005), akaogiite (El Goresy et al. 2010), and Riesite (Tschauner et al. 2020). At 1–2 GPa and under non-hydrothermal conditions, rutile is the stable phase compared to anatase or brookite (Hanaor and Sorrell 2010). However, at a pressure around 4–5 GPa, the polymorph TiO_2-II is the stable phase rather than rutile when temperature is less than 600 ^oC (c.f. Fig. 9 of Hanaor and Sorrell 2010). The presence of rutile in the pseudo-armalcolite grains rather than TiO_2-II implies that the breakdown temperature could be higher than 600 ^oC. The presence of amorphous lamellae in the plagioclase crystal, which probably formed at a shock pressure around 10–30 GPa (Stöffler, 1967), adjacent to the pseudo-armalcolite grain indicates that the plagioclase grain did not experience low-pressure high-temperature annealing, and supports the above assumption that the complete breakdown of armalcolite probably took place when the pressure was still loaded.

IMPLICATIONS

In the present study, we observed two types of micro-textures of armalcolite within an Mg-suite lithic clast in the strongly shock-lithified lunar regolith breccia NWA 8182. One micro-texture is armalcolite decorated with many tiny ilmenite inclusions. The other is pseudo-armalcolite composed of rutile, ilmenite, spinel, and loveringite. We propose that the two micro-textures can be attributed to slow cooling of the source rock at ~1030 ^oC and shock lithification of NWA 8182, respectively. Our observations reveal that strong shock lithification of lunar regolith can cause heterogeneous temperature rises in lithic clasts, with the margin of lithic clasts probably heated up to at least 600 ^{o}C. Although the temperature rise inferred in the present study is at a scale of several micrometers, its presence can affect not only the stability of certain minerals at the margins of lithic clasts (e.g., armalcolite in this study) but also some isotope systems whose closure temperatures are lower than or approaching 600 ^{o}C. For instance, this temperature is high enough to disturb or reset the U-Pb isotopic systematics of apatite, which has a U-Pb closure temperature of 350–550 ^{o}C (Chew and Spikings 2015). In addition, the lithification-induced high temperature is high enough to modify the paleomagnetic records of potential magnetic phases (e.g., pyrrhotite and magnetite) on the surface of the Moon, which have Curie points at around 600 ^{o}C (O’Reilly 1984).

ACKNOWLEDGMENTS AND FUNDING

We appreciate Dr. Axel Wittmann, an anonymous reviewer, and associate Editor Dr. Steven Simon for their constructive comments and suggestions, which greatly improved the quality of the manuscript. This work was financially supported by research grants from the B-type Strategic Priority Program of the Chinese Academy of Sciences (XDB41000000), Natural Science Foundation of China (42025302; 41973061), and a pre-research Project on Civil Aerospace Technologies funded by China National Space Administration (D020204).

REFERENCES CITED

Anderson, A. T., Bunch, T. E., Cameron, E. N., Haggerty, S. E., Boyd, F. R., Finger, L. W., James, O. B., Keil. K, Prinz, M., Ramdohr, P., and El Goresy, A. (1970) Armalcolite: a new mineral from Apollo 11 samples. Proceedings of the Apollo 11 Lunar Science Conference, 1, 55–63.

Brey, G. P., and Kohler, T. (1990) Geothermobarometry in four-phase lherzolites II. New thermobarometers, and practical assessment of existing thermobarometers. Journal of Petrology, 31, 1353–1378.

Chew, D. M., and Spikings, R. A. (2015) Geochronology and thermochronology using apatite: Time and temperature, lower crust to surface. Elements, 11, 189–194.

El Goresy, A., Ramdohr, P., Medenbach, O., and Bernhardt, H. J. (1974) Taurus-Littrow TiO_2-rich basalts: Opaque mineralogy and geochemistry. Proceedings of the Fifth Lunar Conference, 1, 627–652.

El Goresy, A., Dubrovinsky, L., Gillet, P., Graup, G., and Chen, M. (2010) Akaogiite: An ultra-dense polymorph of TiO_2 with the baddeleyite-type structure, in shocked garnet gneiss from the Ries Crater, Germany. American Mineralogist, 95, 892–895.

Friel, J. J., Harker, R. I., and Ulmer, G. C. (1977) Armalcolite stability as a function of pressure and oxygen fugacity. Geochimica et Cosmochimica Acta, 41, 403–410.

Gibbons, R. V., Morris, R. V., and Hörz, F. (1975) Petrographic and ferromagnetic resonance studies of experimentally shocked regolith analogs. Proceedings of the Sixth Lunar Science Conference, 3413–3171.

Haggerty, S. E. (1973) Armalcolite and genetically associated opaque minerals in the lunar sample. Proceedings of the Fourth Lunar Science Conference, 1, 777–797.

Haggerty S. E., Boyd F. R., Bell P. M., Finger L. W., and Bryan W. B. (1970) Opaque minerals and olivine in lavas and breccias from Mare Tranquillitatis. Proceedings of the Apollo 11 Lunar Science Conference, 513–538.

Hanaor, D. A. H., and Sorrell, C. C. (2010) Review of the anatase to rutile phase transformation. Journal of Materials Science, 46, 855–874.

Heiken, G. H., Vaniman, D. T., and French, B. M. (1991) Lunar sourcebook: A user's guide to the Moon. P. 721. Cambridge University Press.

Kesson, S. E., and Lindsley, D. H. (1975) The effects of Al^{3+}, Cr^{3+}, and Ti^{3+} on the stability of armalcolite in vacuum and at 7.5 kbar. Proceedings of the Sixth Lunar Science Conference, 911–920.

Kieffer, S. W. (1975) From regolith to rock by shock. The Moon, 13, 301–320.

Lindsley, D. H. (1991) Experimental Studies of Oxide Minerals. Reviews in Mineralogy and Geochemistry, 25, 69–106.

Lindsley, D. H., Kesson, S. E., Hartzman, M. J., and Cushman, M. K. (1974) The stability of armalcolite: Experimental studies in the system MgO-Fe-Ti-O. Proceedings of the Fifth Lunar Conference, 521–534.

Ma, C., Tschauner, O., Beckett, J. R. Liu, Y., Rossman, G. R., Zhuravlev, K., Prakapenka, V., Dera, P., and Taylor, L. A. (2015) Tissintite, $(Ca,Na,\square)AlSi_2O_6$, a highly-defective, shock-induced, high-pressure clinopyroxene in the Tissint Martian meteorite. Earth and Planetary Science Letters, 422, 194–205.

O'Reilly, W. (1984) Rock and mineral magnetism. Pp. 220. Springer New York.

Papike, J. J., Bence, A. E., and Lindsley, D. H. (1974) Mare basalts from the Taurus-Littrow region of the Moon. Proceedings of the Fifth Lunar Science Conference, 1, 471–504.

Rucks, M. J., Whitaker, M. L., Glotch, T. D., Parise, J. B., Jaret, S. J., Catalano, T., and Dyar, M. D. (2018) Making tissintite: Mimicking meteorites in the multi-anvil. American Mineralogist, 103, 1516–1519.

Rucks, M. J., Glotch, T. D., Whitaker, M. L., Sharp, T. G., Lindsley, D., Catalano, T., & Nekvasil, H. (2019) The behavior of calcium-rich plagioclase under impact relevant conditions and implications for impact studies. 50th Lunar and Planetary Science Conference Abstract#2691.

Ruzicka, A., Grossman, J., Bouvier, A., and Agee, C. B. (2017) The Meteoritical Bulletin, No. 103. Meteoritics & Planetary Science, 52, 1014.

Schaal, R. B., and Hörz, F. (1980) Experimental shock metamorphism of lunar soil. Geochimica et Cosmochimica Acta, 14, 167–196.

Sharp, T. G., and DeCarli, P. S. (2006) Shock effects in meteorites. Meteorites and the Early Solar System II. p.653–677. University of Arizona Press.

Shearer, C. K., Elardo, S. M., Petro, N. E., Borg, L. E., and McCubbin, F. M. (2015) Origin of the lunar highlands Mg-suite: An intergrated petrology, geochemistry, chronology, and remote sensing perspective. American Mineralogist, 100, 294–325.

Simonds, C. H. (1973) Sintering and hot pressing of Fra Mauro composition glass and the lithification of lunar breccias. American Journal of Science, 273, 428–439.

Simonds, C. H., Warner, J. L., Phinney, W. C., and McGee, P. E. (1976) Thermal model for impact breccia lithification: Manicouagan and the moon. Proceedings of the Seventh Lunar Conference, 2, 2509–2528.

Spray, J. G. (2016) Lithification mechanisms for planetary regoliths: The glue that binds. Annual Review of Earth and Planetary Sciences, 44, 139–174.

Stanin, F. T., and Taylor L. A. (1979) Armalcolite/Ilmenite: Mineral chemistry, paragenesis, and origin of textures. Proceedings of the Tenth Lunar Science Conference, 383–405.

Steele, I. M., and Smith, J. V. (1972) Occurrence of diopside and Cr-Zr-armalcolite on the Moon. Nature Physical Science, 237, 105–106.

Stöffler, D. (1967) Deformation und Umwandlung von Plagioklas durch Stoßwellen in den Gesteinen des Nördlinger Ries. Contribution to Mineralogy and Petrology, 16, 51-83.

Stöffler, D., Hamann, C., and Metzler, K. (2018) Shock metamorphism of planetary silicate rocks and sediments: Proposal for an updated classification system. Meteoritics & Planetary Science, 53, 5–49.

Taylor, G. J., Warren, P., Ryder, G., Delano, J., Pieters, C., and Lofgren, G. (1991) Lunar rocks. Lunar sourcebook: A user's guide to the Moon. Pp. 183–284. Cambridge University Press.

Thacker, C., Liang, Y., Peng, Q., and Hess, P. (2009) The stability and major element partitioning of ilmenite and armalcolite during lunar cumulate mantle overturn. Geochimica et Cosmochimica Acta, 73, 820–836.

Treiman, A. H., and Gross, J. (2015) A rock fragment related to the magnesian suite in lunar meteorite Allan Hills (ALHA) 81005. American Mineralogist, 100, 414–426.

Tschauner, O., Ma, C., Lanzirotti, A., and Newville, M. G. (2020) Riesite, a new high pressure polymorph of TiO_2 from the Ries impact structure. Minerals, 10, 78. Doi:10.3390/min10010078.

Uhlmann, D. R., Klein, L., and Hopper, R. W. (1975) Sintering, crystallization, and breccia formation. The Moon, 13, 277–284.

Warner, J. L. (1972) Apollo 14 breccias: Metamorphic origin and classification. Abstract of the Lunar and Planetary Science Conference, 3, 782.

Warner, J. L, Simonds, C. H., and Phinney, W. C. (1973) Apollo 16 rocks: Classification and petrogenetic model. Proceedings of the Fourth Lunar Science Conference, 4, 481–503.

Wells, P. R. A. (1977) Pyroxene thermometry in simple and complex systems. Contributions to Mineralogy and Petrology, 62, 129–139.

Williams, K. L., and Taylor, L. A. (1974) Optical properties and chemical compositions of Apollo 17 armalcolites. Geology, 5–8.

Williams, R. J. (1972) The lithification and metamorphism of lunar breccias. Earth and Planetary Science Letters, 16, 250–256.

Wu, X., Meng, D., and Han, Y. (2005) α-PbO_2-type nanophase of TiO_2 from coesite-bearing eclogite in the Dabie Mountains, China. American Mineralogist, 90, 1458–1461.

Zhang, A. C., Jiang, Q. T., Tomioka, N., Guo, Y. J., Chen, J. N., Li, Y., Sakamoto, N., and Yurimoto, H. (2021) Widespread Tissintite in strongly shock-lithified lunar regolith breccias. Geophysical research letters, 48, e2020GL091554.

Zhang, A. C., Pang, R. L., Sakamoto, N., and Yurimoto, H. (2020) The Cr-Zr-Ca armalcolite in lunar rocks is loveringite: Constraints from electron backscatter diffraction measurements. American Mineralogist, 105, 1021–1029.

Figure Captions

Figure 1. BSE images of two represenative vesicular glassy regions (a and b) in NWA 8182. The fine-grained matrix material in (a) and (b) has transformed into glass. Rounded and elongate vesicles are common in the glassy regions.

Figure 2. False-color images of X-ray elemental mapping results of Clast-20. (a) Combined Mg-Ca-Al image shows the distribution of olivine, enstatite, augite grains in Clast-20. (b) Combined Ti-Cr-Fe image shows the distribution of armalcolite, loveringite, chromite, and ilmenite in Clast-20. Ilmenite grains in Clast-20 are indicated by the dashed circles. Ol: olivine; En: enstatite; Aug: augite; An: anorthite; Arm: armalcolite; pArm: pseudo-armalcolite; Lvg: loveringite; Chr: chromite; Ilm: ilmenite.

Figure 3. BSE images of normal armalcolite in Clast-20. (a–b) Tiny ilmenite inclusions in armalcolite, which is generally homogeneous. Note the orientated distribution of ilmenite grains. (c) An armalcolite grain intergrown with a loveringite grain. The armalcolite grain is about 10 μm away from the tissintite- and vesicle-bearing glassy matrix. The dash-line rectangle shows the location of FIB-1. (d) The zoom-in image of the armalcolite grain shown in (c). Note the heterogeneous Z-contrast of armalcolite in BSE image. Ilm: ilmenite; Arm: armalcolite; Tst: tissintite; Lvg: loveringite.

Figure 4. TEM observation results of FIB-1. (a) HAADF-STEM image; (b) X-ray elemental mapping results (Mg, Fe, Al, and Ti) showing the distribution of armalcolite and ilmenite; (c) Bright field TEM image; (d) A SAED pattern of armalcolite in FIB-1; (e) FFT pattern of ilmenite in FIB-1. Arm: armalcolite; Ilm: ilmenite.

Figure 5. BSE images of pseudo-armalcolite in Clast-20. (a) Clast-20 is surrounded by thick, vesicle-rich glassy matrix. (b) The zoom-in image of the rectangle shown in (a).

The dash-line rectangle shows the location of FIB-2 section. (c–d) The two pseudo-armalcolite grains show heterogeneous Z-contrasts in BSE images. pArm: pseudo-armalcolite; Tst: tissintite; An: anorthite; Aug: augite; En: enstatite.

Figure 6. BSE image (a) and low-resolution X-ray elemental mapping results (b–f) of one pseudo-armalcolite grain in Clast-20. (a) The pseudo-armalcolite grain contains many tiny, dark grains. (b–d) Ti, Fe, and Mg show large chemical variations within the pseudo-armalcolite grain. (e–f) A tiny Al- and Cr-rich phase is present in the grain, generally corresponding to the dark phase in (a).

Figure 7. TEM observation results of the pseudo-armalcolite in FIB-2 section. (a) HAADF-STEM image; (b) X-ray elemental (Mg, Fe, Al, and Ti) mapping results showing the distribution of different phases; (c) False-color image of Ca distribution in FIB-2; (d) Bright field TEM image showing a local region containing loveringite. Ilm: ilmenite; Rt: rutile; Spl: spinel; Lvg; loveringite; An: anorthite; Aug: augite.

Figure 8. Structural characterization results of ilmenite, rutile, spinel, and loveringite in FIB-2. (a), (b), and (d) are SAED patterns of ilmenite, rutile, and loveringite. (c) is Fast Fourier Transfer result based on a high-resolution TEM image of spinel. Ilm: ilmenite; Rt: rutile; Spl: spinel; Lvg: loveringite.

Figure 9. STEM-EDS spectrum of spinel in the pseudo-armalcolite grain (FIB-2).

Figure 10. Microscopic observation results of an anorthite grain in contact with a pseudo-armalcolite in FIB-2 section. (a) Bright filed image taken in field-emission scanning electron microscope after FIB preparation. Note the parallel features in the anorthite grain. (b) High resolution (HR) TEM image of anorthite in the rectangle region

DOI: https://doi.org/10.2138/am-2022-8790. http://www.minsocam.org/

outline in (a). Note the amorphous regions between crystalline anorthite regions. An: anorthite; Rt: rutile; Lvg: loveringite.

Figure 11. Schematic phase diagram of the MgO-Fe-Ti-O system, based on Lindsley (1991). The red and blue arrows indicate two breakdown reactions of nonstoichiometric armalcolite at two different stages, respectively. Arm: armalcolite; Ilm: ilmenite; Rt: rutile.

Table 1. EPMA compositions of normal and pseudo-armalcolite in Clast-20

	Normal armalcolite							Pseudo-armalcolite	
SiO_2	0.08	0.07	0.11	0.16	0.10	0.16	0.08	0.25	0.20
TiO_2	73.52	73.78	73.57	72.64	72.96	72.91	73.31	73.25	73.62
ZrO_2	0.54	0.48	0.51	0.48	0.55	0.94	0.68	0.49	0.48
Al_2O_3	0.81	0.76	1.11	0.89	0.33	1.00	0.99	1.26	1.07
Cr_2O_3	2.00	1.25	1.95	1.03	2.02	1.92	1.60	1.64	1.56
MgO	10.16	9.84	10.55	9.78	9.23	10.24	10.43	9.41	9.44
FeO	12.44	13.57	12.19	14.43	14.33	12.02	11.99	11.48	11.35
MnO	0.08	0.08	0.07	0.07	0.08	0.06	0.08	0.08	0.09
CaO	0.63	0.43	0.59	0.60	0.43	0.58	0.42	0.70	0.62
Total	100.26	100.26	100.65	100.08	100.03	99.83	99.58	98.56	98.43
Si	0.003	0.003	0.004	0.006	0.004	0.006	0.003	0.009	0.007
Ti	1.954	1.966	1.943	1.947	1.961	1.943	1.956	1.969	1.981
Zr	0.009	0.008	0.009	0.008	0.010	0.016	0.012	0.009	0.008
Al	0.034	0.032	0.046	0.037	0.014	0.042	0.041	0.053	0.045
Cr	0.056	0.035	0.054	0.029	0.057	0.054	0.045	0.046	0.044
Mg	0.540	0.525	0.557	0.524	0.496	0.546	0.556	0.506	0.508
Fe	0.367	0.402	0.358	0.430	0.428	0.356	0.355	0.343	0.339
Mn	0.002	0.003	0.002	0.002	0.003	0.002	0.002	0.002	0.003
Ca	0.024	0.016	0.022	0.023	0.016	0.022	0.016	0.027	0.024
Cations	2.989	2.989	2.994	3.006	2.990	2.987	2.987	2.964	2.959
Mg#	0.60	0.57	0.61	0.55	0.54	0.61	0.61	0.60	0.60

Notes: Normal armalcolite was measured with a focused beam, while pseudo-armalcolite was measured with a defocused beam (3 μm in diameter).

Cations are calculated on the basis of 5 oxygen atoms.

Table 2. STEM-EDS compositions of ilmenite in normal armalcolite (FIB-1) and pseudo-armalcolites (FIB-2)

	Ilmenite in FIB-1		Ilmenite in FIB-2	
TiO_2	58.1	58.0	58.5	58.7
MgO	15.1	15.5	21.5	21.7
FeO	26.9	26.4	20.1	19.6
Total	100.1	99.9	100.1	100.0
Ti	0.99	0.99	0.96	0.96
Mg	0.40	0.41	0.55	0.55
Fe	0.67	0.66	0.48	0.47
Cations	2.06	2.05	1.99	1.99
Mg#	0.37	0.38	0.53	0.54

Notes: The STEM-EDS data have been calibrated with the k factors for Ti, Mg, and Fe based on the data of armalcolite that has been measured with both EMPA and STEM-EDS.

Cations in ilmenite are calculated on the basis of 3 oxygen atoms.

Figure 1

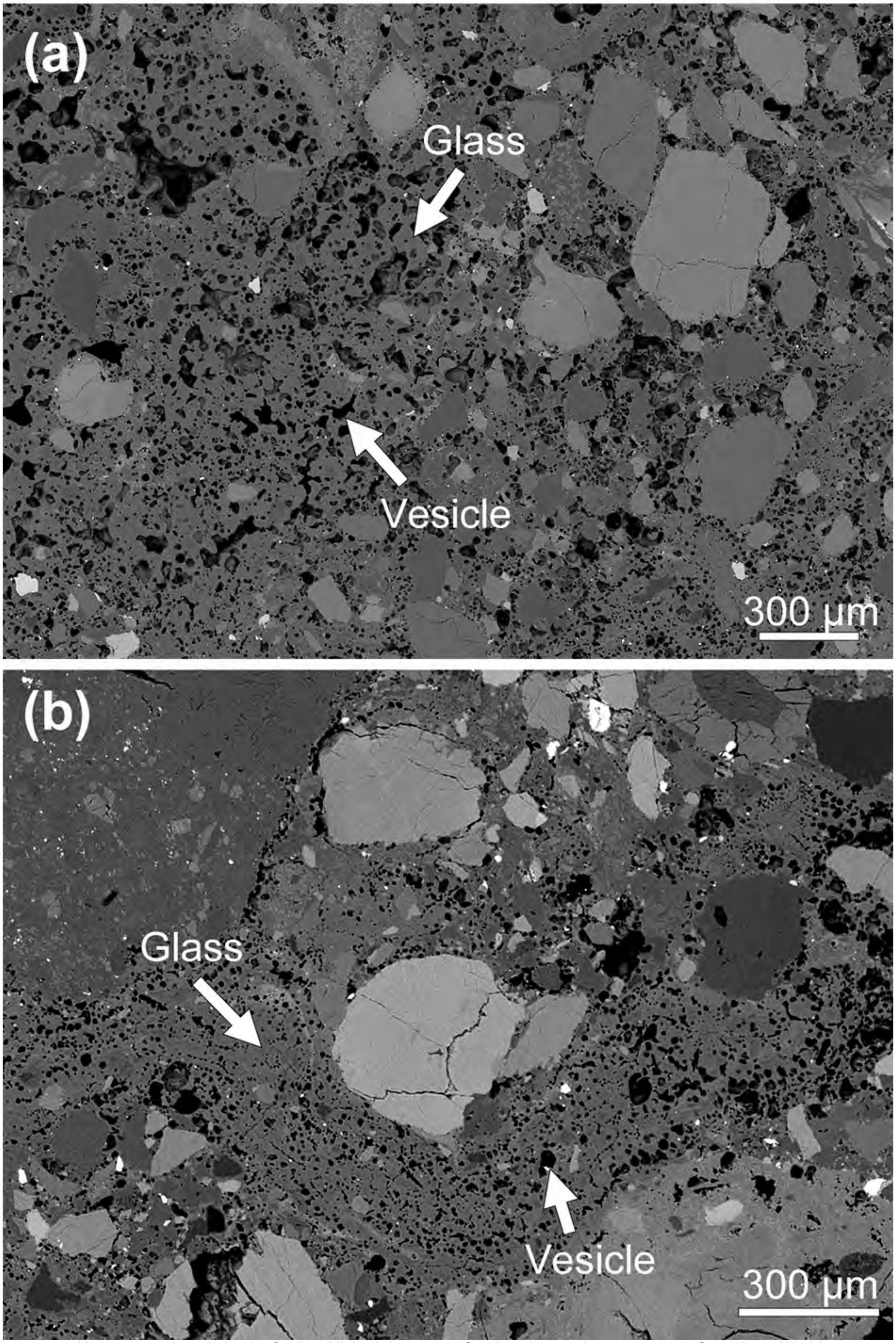

This is the peer-reviewed, final accepted version for American Mineralogist, published by the Mineralogical Society of America.
The published version is subject to change. Cite as Authors (Year) Title. American Mineralogist, in press.
DOI: https://doi.org/10.2138/am-2022-8790. http://www.minsocam.org/

Figure 2

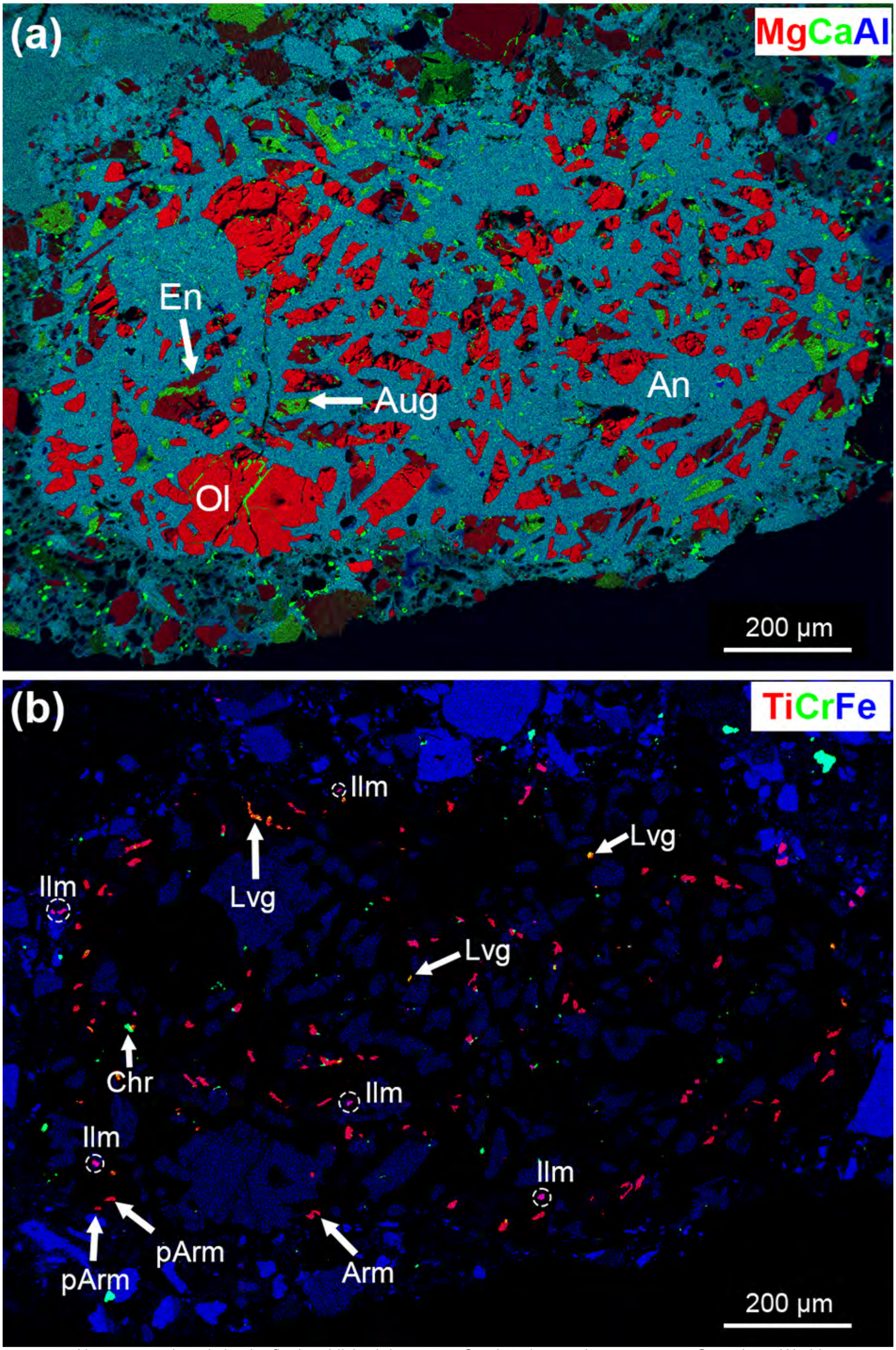

Figure 3

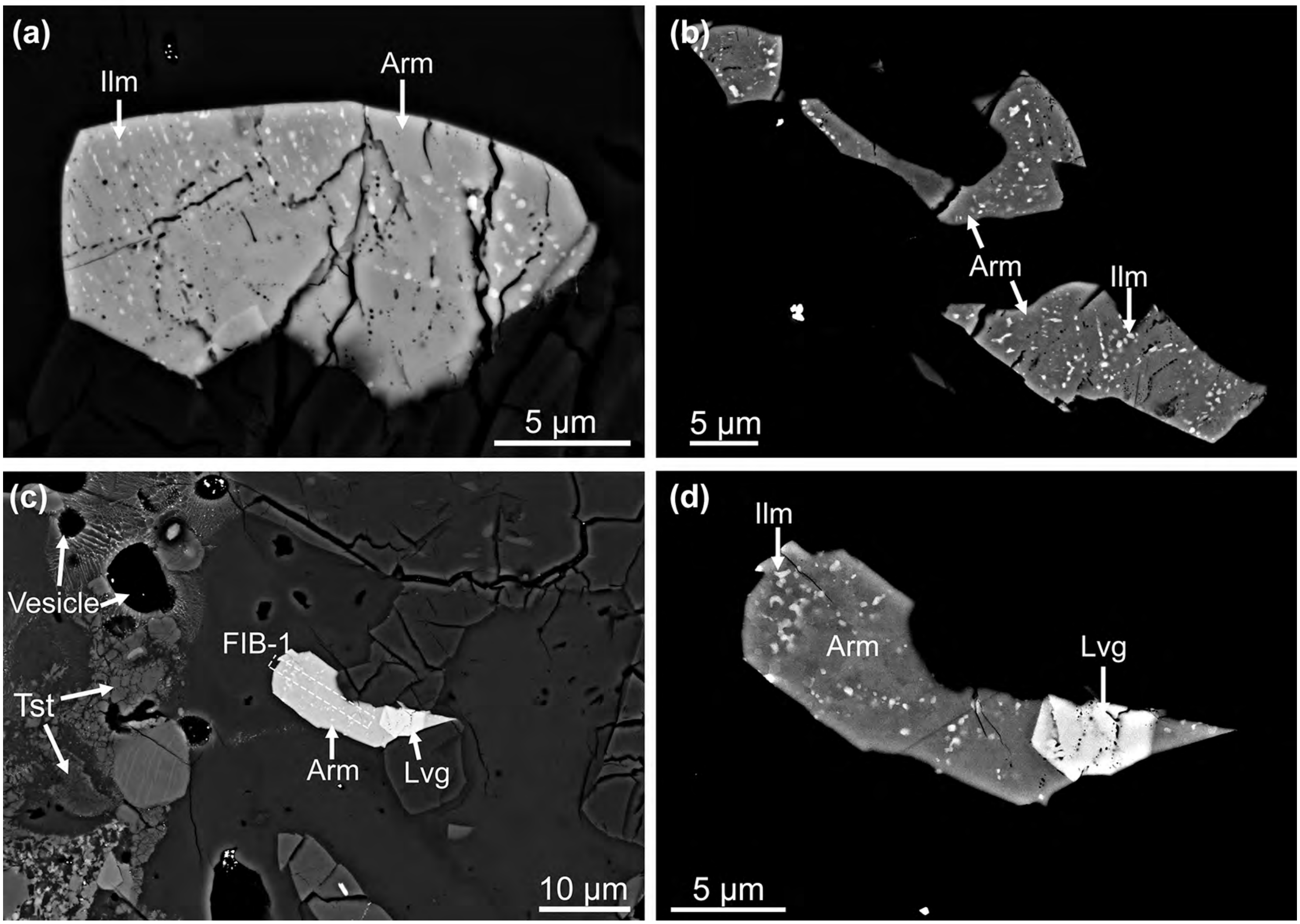
(a)
Ilm
Arm
5 µm
(b)
Arm
Ilm
5 µm
(c)
Vesicle
Tst
FIB-1
Arm
Lvg
10 µm
(d)
Ilm
Arm
Lvg
5 µm

Figure 4

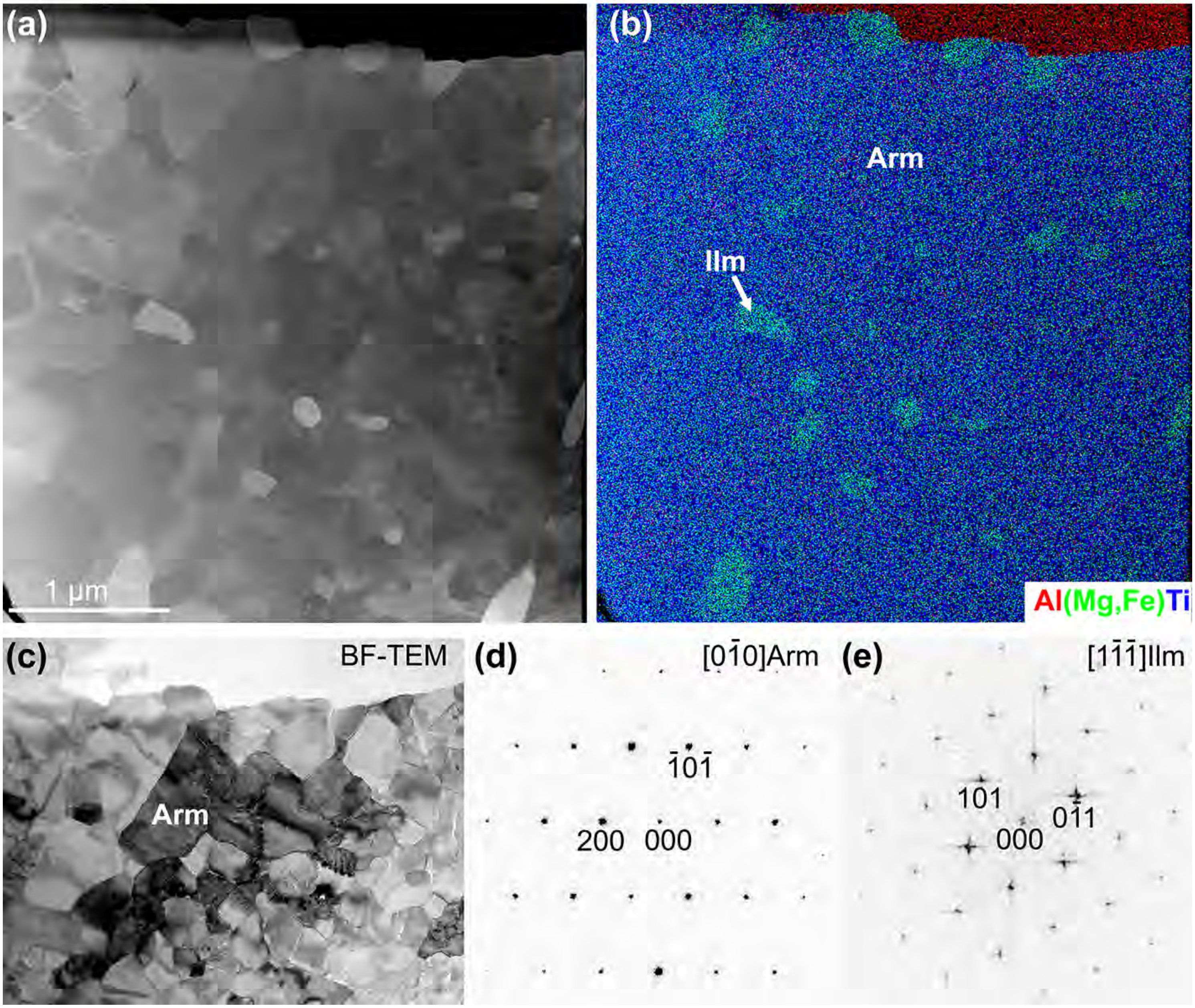
(a)
1 μm
(b)
Arm
Ilm
Al(Mg,Fe)Ti
(c)
BF-TEM
Arm
(d)
[0$\bar{1}$0]Arm
$\bar{1}$0$\bar{1}$
200
000
(e)
[1$\bar{1}\bar{1}$]Ilm
101
0$\bar{1}$1
000

Figure 5

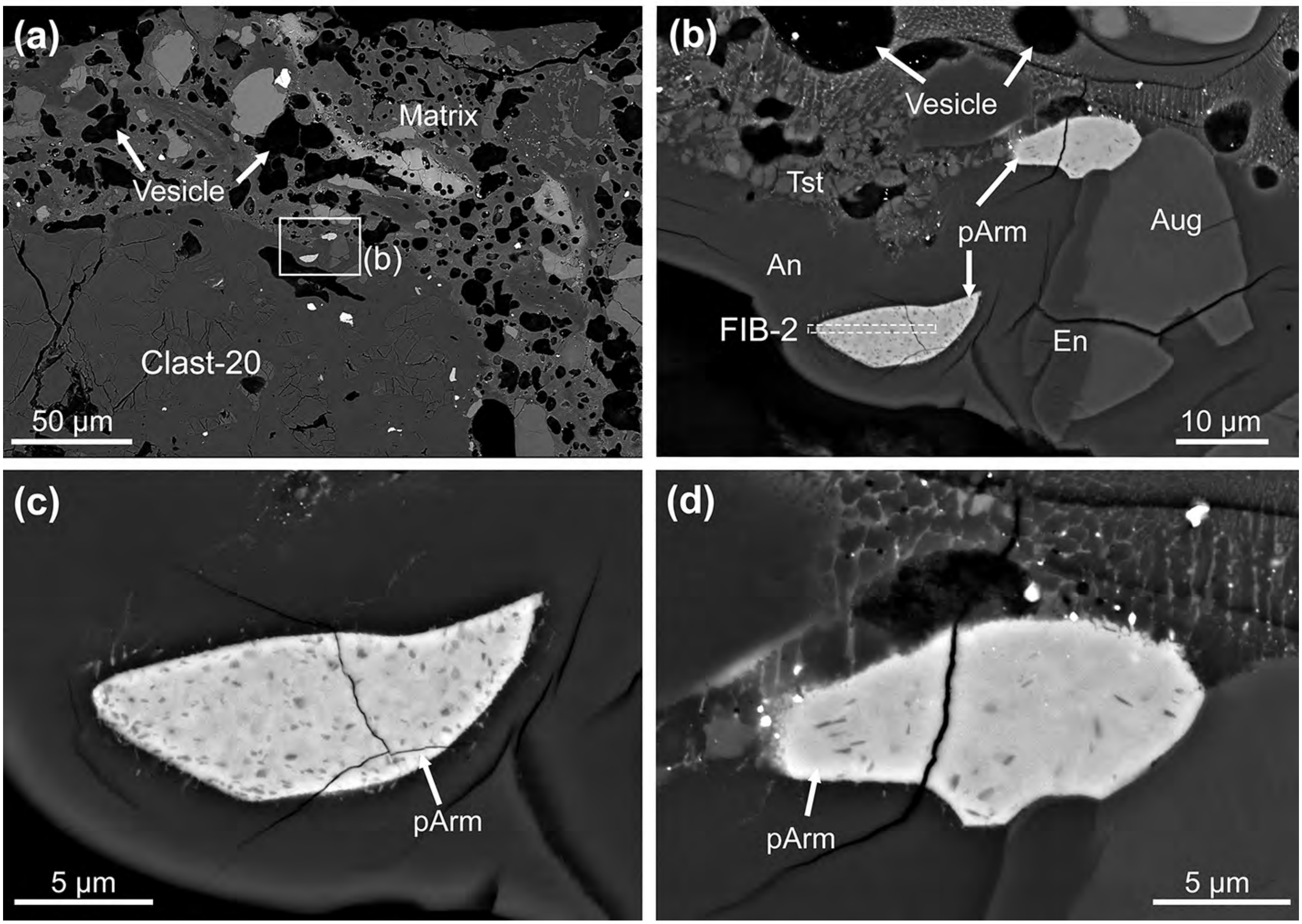
(a)
Matrix
Vesicle
(b)
Clast-20
50 µm
(b)
Vesicle
Tst
pArm
Aug
An
FIB-2
En
10 µm
(c)
pArm
5 µm
(d)
pArm
5 µm

Figure 6

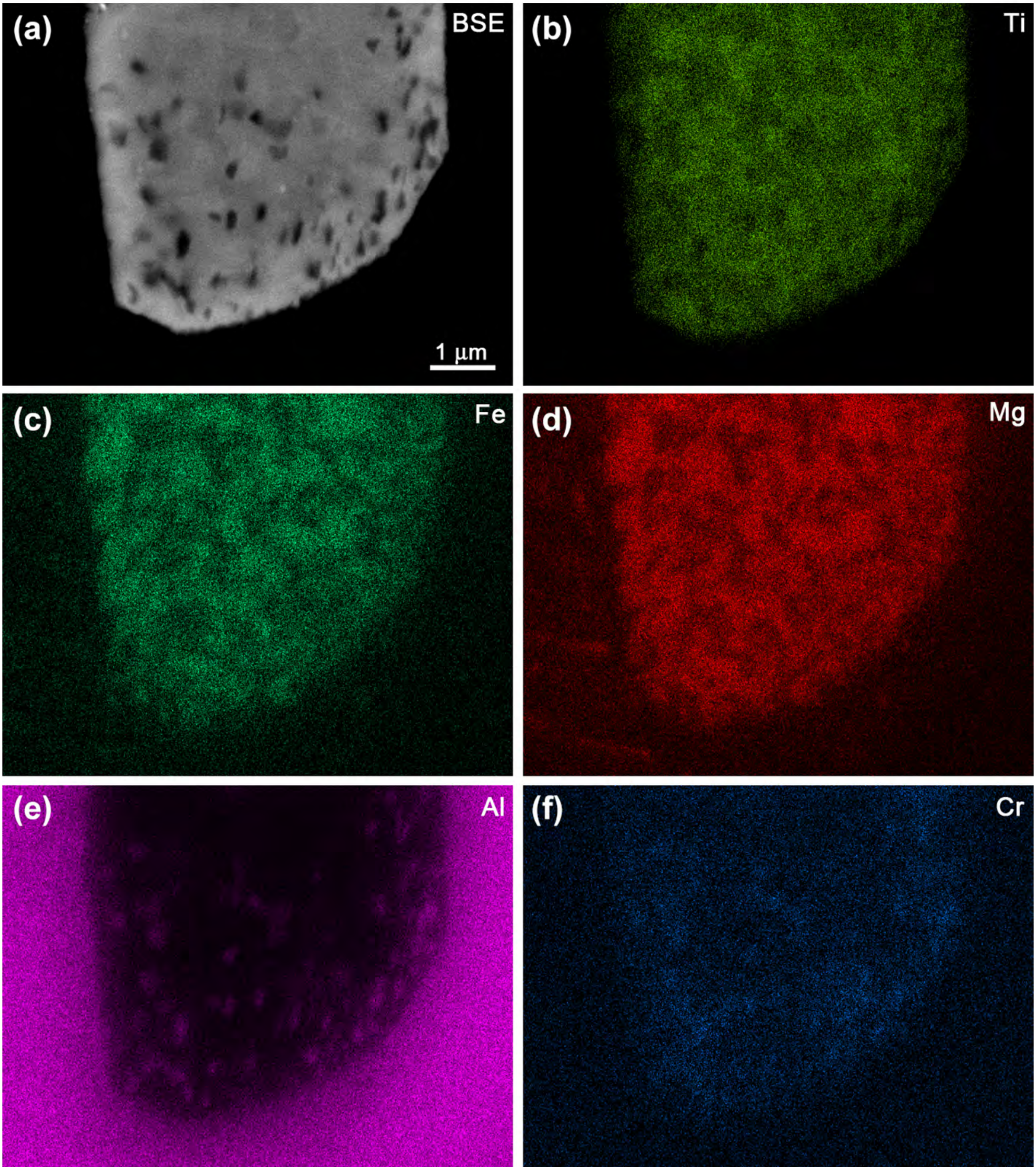

Figure 7

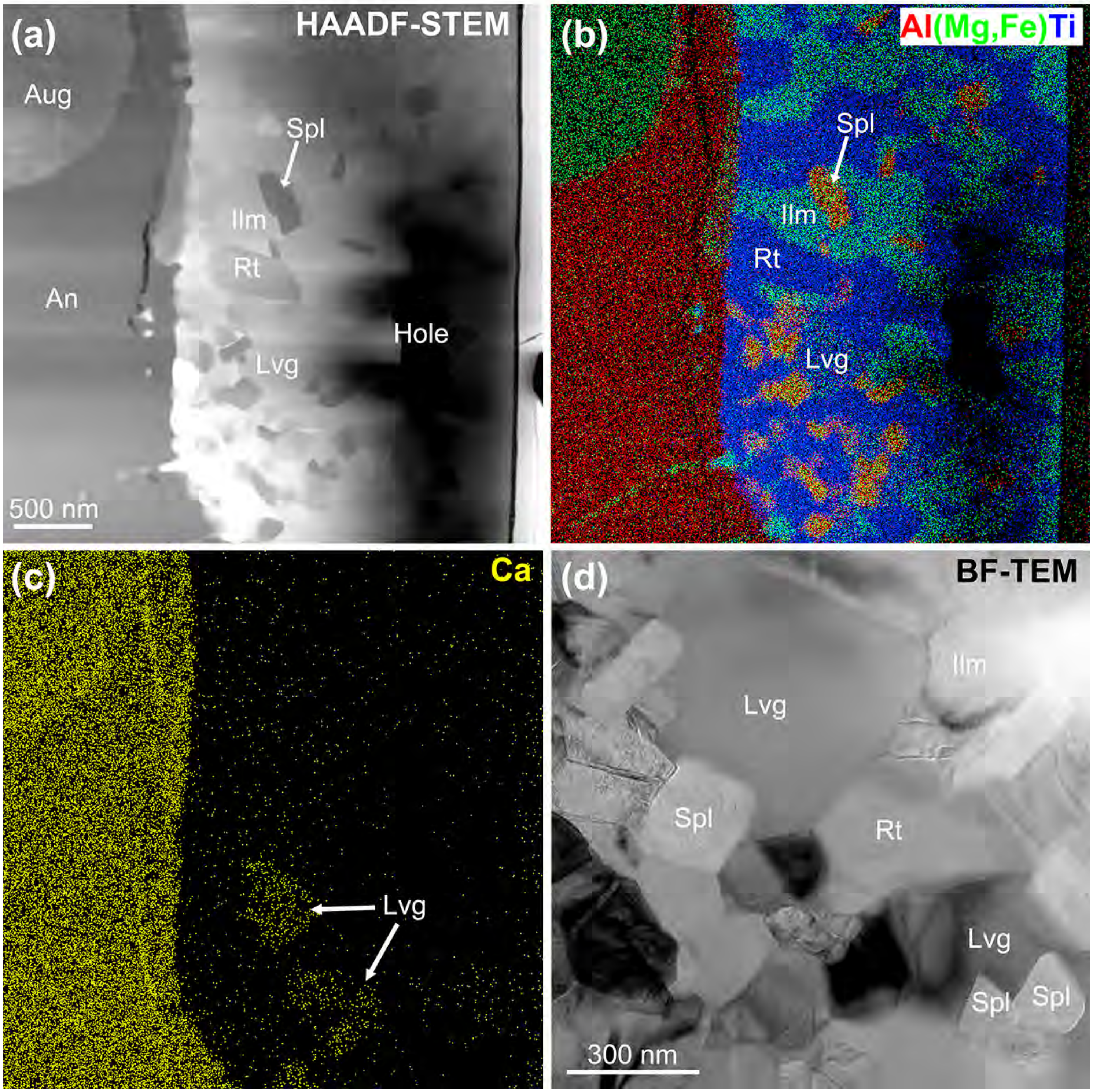
(a)
HAADF-STEM
Aug
Spl
Ilm
Rt
An
Hole
Lvg
500 nm
(b)
Al(Mg,Fe)Ti
Spl
Ilm
Rt
Lvg
(c)
Ca
Lvg
(d)
BF-TEM
Ilm
Lvg
Spl
Rt
Lvg
Spl
Spl
300 nm

Figure 8

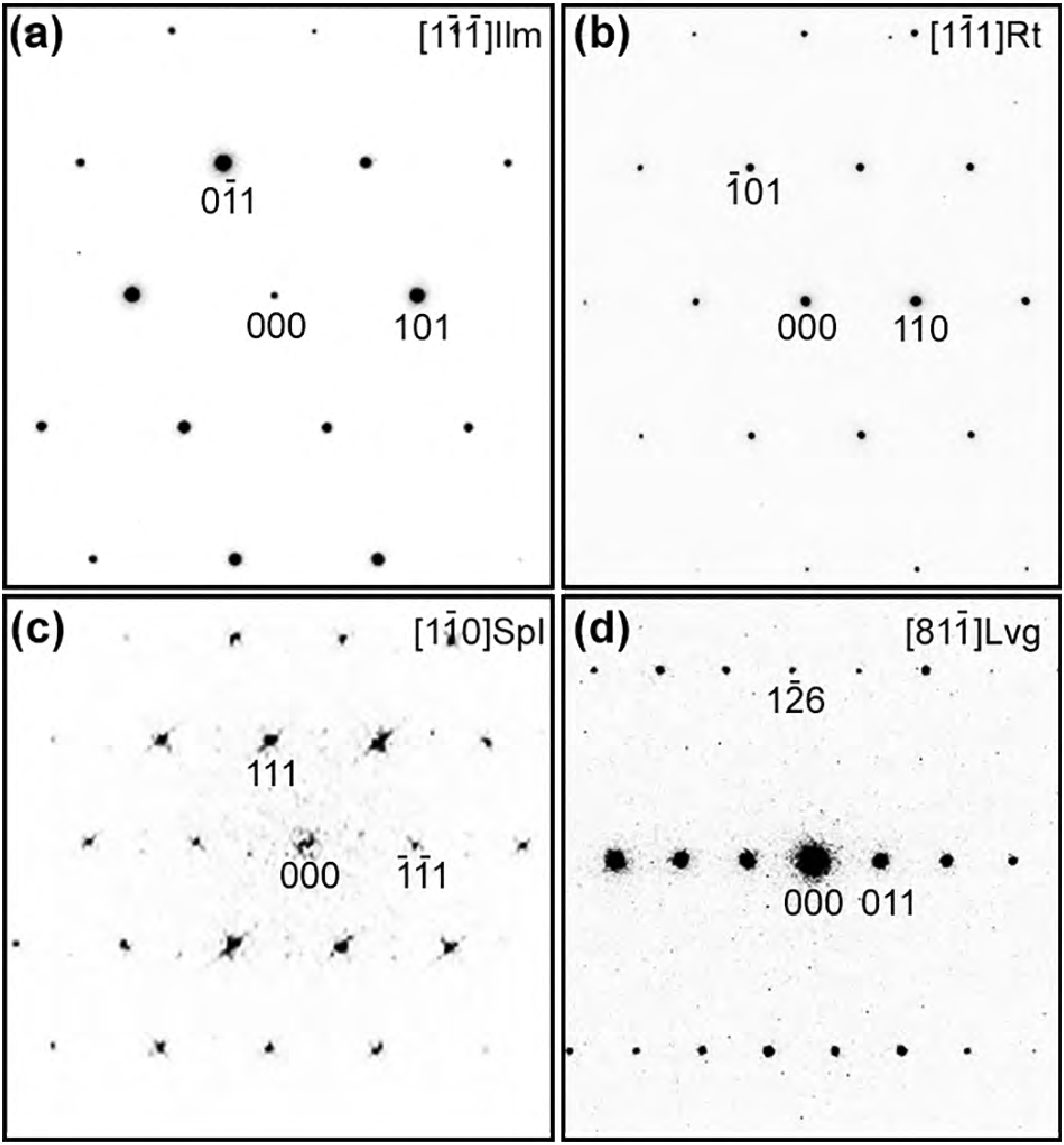
(a)
[1$\bar{1}\bar{1}$]Ilm
0$\bar{1}$1
000
101
(b)
[1$\bar{1}$1]Rt
$\bar{1}$01
000
110
(c)
[1$\bar{1}$0]Spl
111
000
$\bar{1}\bar{1}$1
(d)
[81$\bar{1}$]Lvg
1$\bar{2}$6
000
011

Figure 9

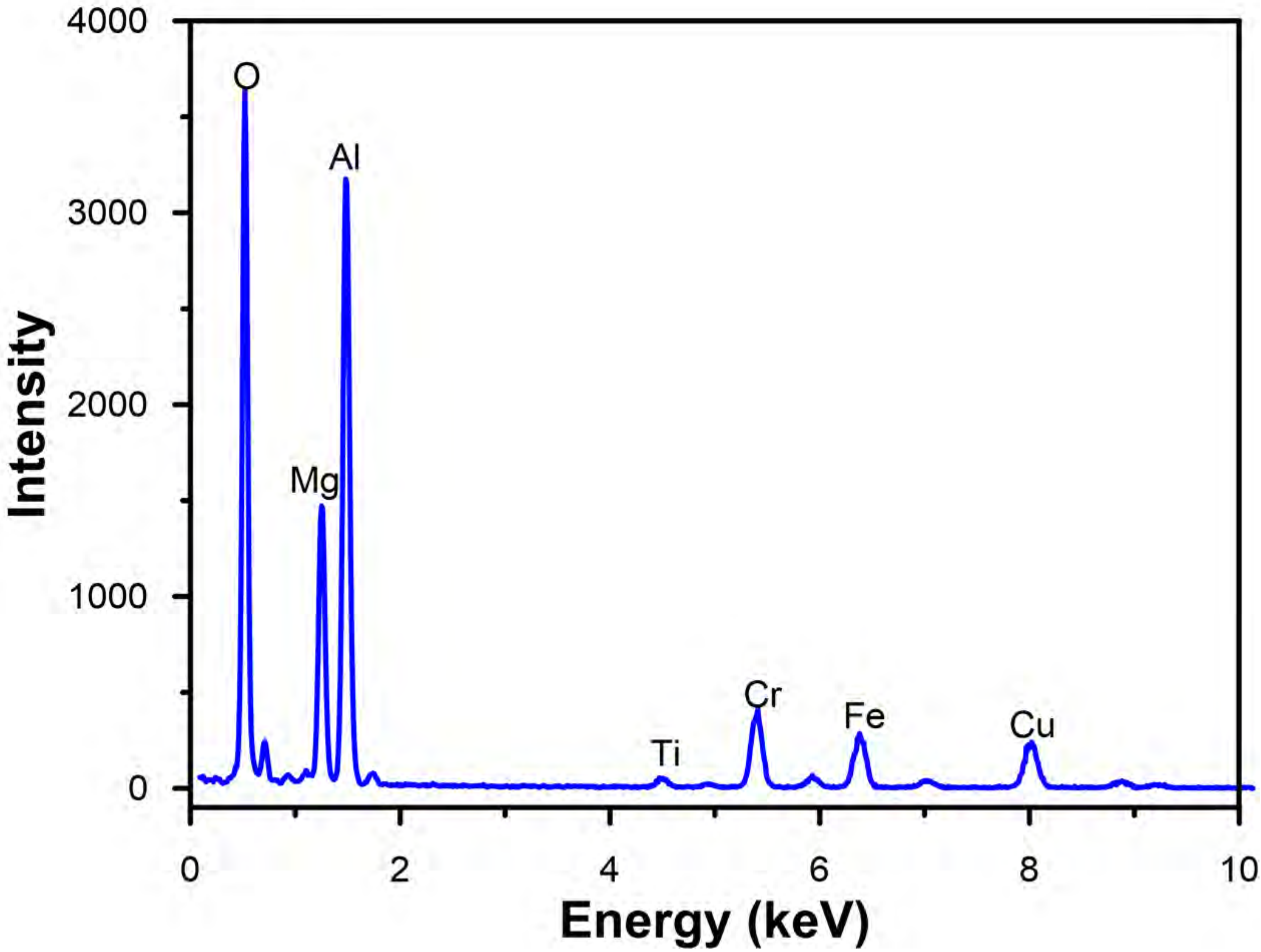
4000
3000
2000
1000
0
Intensity
O
Al
Mg
Ti
Cr
Fe
Cu
0
2
4
6
8
10
Energy (keV)

Figure 10

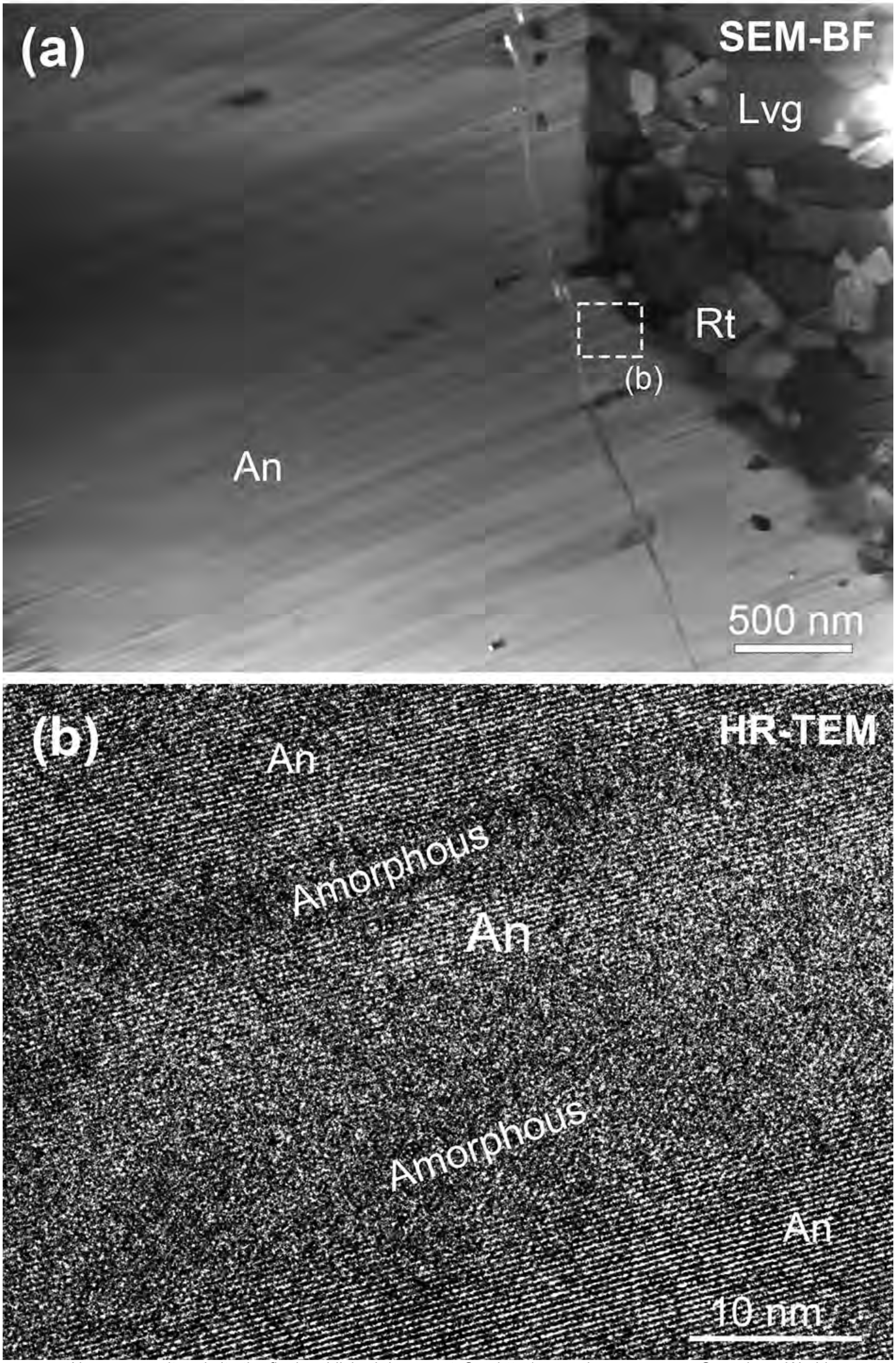
(a)
SEM-BF
Lvg
Rt
(b)
An
500 nm
(b)
HR-TEM
An
Amorphous
An
Amorphous
An
10 nm

Figure 11

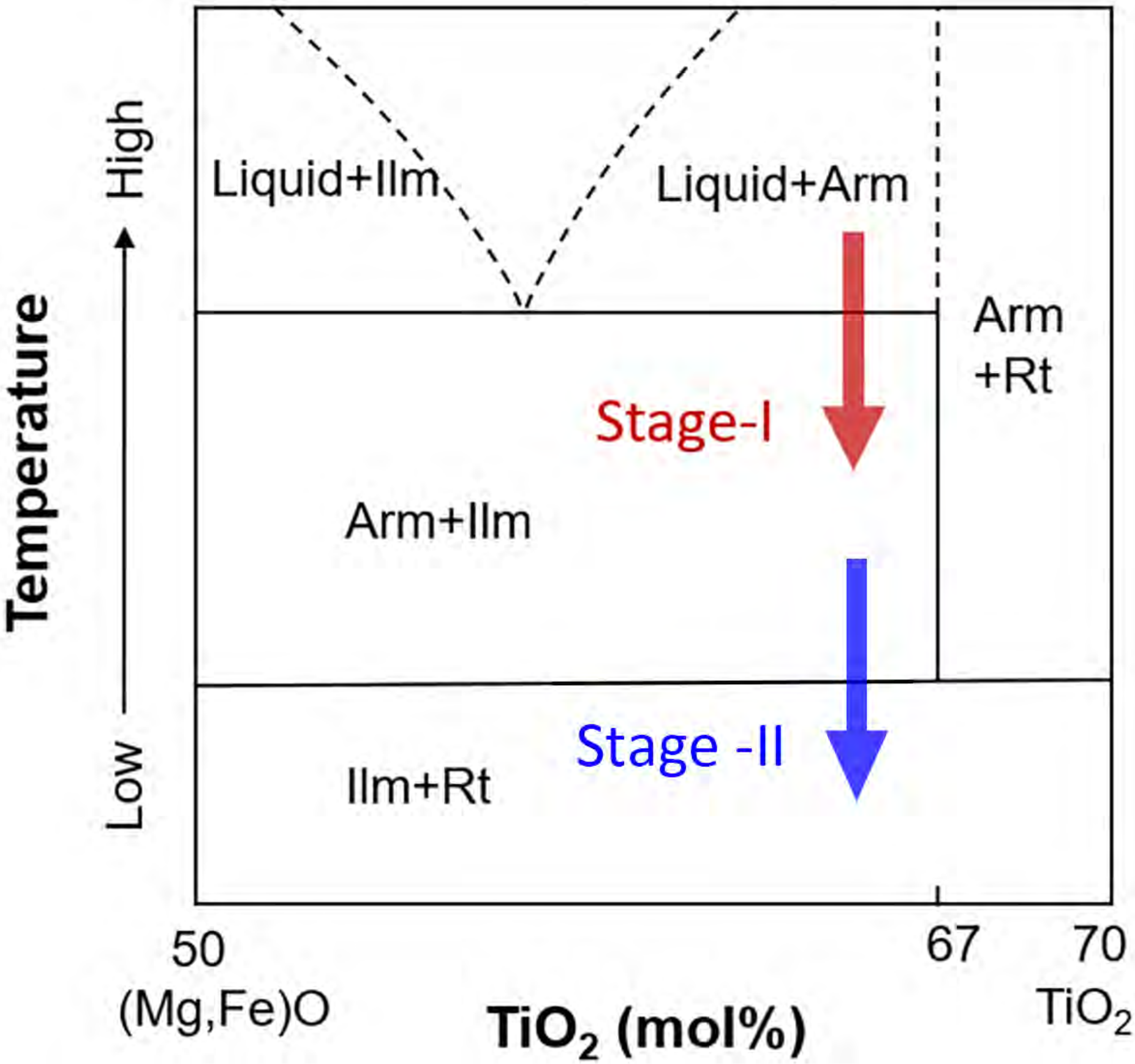
Liquid+Ilm
Liquid+Arm
Arm
+Rt
Stage-I
Arm+Ilm
Stage -II
Ilm+Rt
High
Low
Temperature
50
(Mg,Fe)O
67
70
TiO2
TiO2 (mol%)